(Received 11 September 2024, Accepted 11 October 2024, Scheduled 21 October 2024)

Design of Compensated PLL for Position Sensorless Drives of PMSMs

Lin Han[1], Shanshan Wang[1,*], Zhonggen Wang[1], Xiaobing Zhu[1], and Wenyan Nie[2]

[1]*School of Electrical and Information Engineering, Anhui University of Science and Technology, Huainan 232001, China*
[2]*School of Mechanical and Electrical Engineering, Huainan Normal University, Huainan 232001, China*

ABSTRACT: To filter out the high harmonic content of the back electromotive force (EMF) in the conventional sliding mode observer (SMO), a novel flux SMO (FSMO) is designed in this paper. The feedback matrix is designed to replace the external filter or other modules, and its higher-order feedback characteristics further enhance the convergence of the FSMO. The Lyapunov function is used to assess the stability of the FSMO. Importantly, a compensated phase-locked loop (CPLL) with an angular compensation strategy is used to extract both position and speed information, resulting in less speed fluctuation and lower position estimation error. Furthermore, the simulation model and experimental platform are developed to evaluate the reliability of the proposed method. Both simulated and experimental results confirm that the proposed hybrid control algorithm performs well in both steady state and dynamic one, high or low speed of the system, with suppressed harmonics of 50.1% and 7.3%, respectively, and an improved response time of 54.1%, providing a concrete program for sensorless control of permanent magnet synchronous motors (PMSMs).

1. INTRODUCTION

Permanent magnet synchronous motors (PMSMs) have been widely applied in computer numerical control (CNC) grinding machines [1] or other intelligent software, due to their advantages, such as high torque output, elevated power density, and exceptional energy efficiency. Field-oriented control (FOC) is a commonly used strategy for PMSM drives that requires precise rotor position information. However, some mechanical components, such as encoders, resolvers, and Hall sensors, may introduce mechanical noise, reducing system stability [2]. Therefore, position sensorless control methods for PMSM have become a popular topic in many studies.

Position sensorless methods can be classified into two types: high-frequency signal injection [3] for zero or ultra-low speed and back electromotive force (EMF) extraction for medium-high speed, which includes sliding mode observer (SMO), model reference adaptive system [4], and extend Kalman filter [5]. SMO is widely used for position sensorless control of PMSMs due to its high robustness, immunity to external disturbances, and parameter tunability.

In the conventional SMO method, the switching function is always used to extract the back EMF, and the inherent discontinuous characteristics of the switching function can lead to significant challenges in the modulation process, causing the system to chatter. Recognizing these issues, [6] introduces a sigmoid function as a replacement for the discontinuous function in fault-tolerant permanent magnet motors used in electric ship propulsion systems. Meanwhile, a control method that combines the piecewise root function with a low-pass filter (LPF) has been introduced in [7], and the limitations of the LPF cause the inaccuracy of the position estimates. To address this, Ding et al. present an adaptive filter designed to improve the robustness against system uncertainties [8]. Furthermore, to tackle the phase lag issue in back EMF estimation, a phase-shifting method is proposed in [9], which helps mitigate phase lag and enhances the accuracy of back EMF estimates. Although these advancements have made significant strides, they still face limitations when dealing with inverter nonlinearity. As noted in [10], neglecting the nonlinear characteristics of the inverter can result in observed currents containing high harmonics, which adversely affects the accuracy of back EMF estimates. To tackle this challenge, some researchers proposed a sensorless control method based on flux linkage. In [11], a second order generalized integral flux observe is used for estimating rotor flux linkages of PMSMs, in which the dc component is limited to a certain value. Given the urgent need to further improve the accuracy of rotor flux estimates, a novel approach that integrates rotor flux estimation with a sliding mode observer has been proposed by other researchers. In [12], an adaptively tuned observer gain method is proposed that iteratively employs a flux sliding mode observer within one current cycle, improving position tracking ability and reducing chatter phenomena. However, the performance of this observer is limited due to its dependency on parameters. To address this issue, a modified flux SMO with a parameter identification algorithm is proposed, significantly improving the system's robustness and parameter identification capability [13]. Building on this approach, [14] introduces a real-time adjustment of the observer gain to improve position estimation. Additionally, a control strategy that uses simultaneous rotor position and flux estimation to eliminate flux warping caused by inverter nonlinearity is proposed [15].

* Corresponding author: Shanshan Wang (ShanshanWang9090@163.com).

The arc tangent function is commonly used to extract position and velocity information [16], but its inherent limitations can cause singularity problems. As a result, phase-locked loop (PLL) control methods are widely used for position estimation [17]. In [18], the authors describe the adoption of a second-order generalized integrator within the PLL to eliminate low harmonics and enhance position estimation capability. Additionally, the transfer function of a quadrature PLL is discussed for rotor position estimation [19], although adjusting the PI parameters in this controller can be challenging.

Unlike the conventional method that combines the sliding mode observer with a phase-locked loop, this paper presents a novel method that integrates a flux sliding mode observer (FSMO) with a compensated phase-locked loop (FSMO-CPLL) for the sensorless position control of PMSM. The main contributions of this strategy can be summarized as follows:

1) Because conventional SMOs contain a high harmonic of back EMF, an FSMO is designed to minimize rotor flux linkage distortion. The feedback matrix is designed to replace an external filter, and the stability of the FSMO is investigated.
2) When being combined with an angle compensation strategy, the proposed compensated phase-locked loop (CPLL) significantly reduces phase lag and improves rotor position stability. This improvement results in more accurate motor control, particularly in dynamic scenarios.
3) Rotor position and speed estimation are performed on a PMSM-driven platform; experimental results demonstrate that the proposed method has excellent performance in eliminating system chatter.

2. CONVENTIONAL SMO

As mentioned in the introduction, sliding mode control is a variable structure control that can be implemented for both speed tracking and position tracking. Specifically, for position tracking, a sliding mode control law is designed by constructing the stator current equation to estimate the back-EMF. For instance, Liu et al. [20] integrated the conventional sliding mode observer with a phase-locked loop, creating an SMO-PLL system to extract rotor information. In this system, the SMO is utilized to reconstruct the back-EMF using phase voltages and currents, while the PLL tracks the rotor position.

Based on the analyses and taking the surface-mounted PMSM as the subject of this article, it is assumed that the stator is a three-phase symmetrical winding, and the stator current equation in the stationary coordinate system is as follows:

$$\begin{cases} \frac{di_\alpha}{dt} = -\frac{R}{L_s} i_\alpha + \frac{1}{L_s} u_\alpha - \frac{1}{L_s} E_\alpha \\ \frac{di_\beta}{dt} = -\frac{R}{L_s} i_\beta + \frac{1}{L_s} u_\beta - \frac{1}{L_s} E_\beta \end{cases} \tag{1}$$

where u_α, u_β, i_α and i_β are stator voltage and stator current; R and L_s are resistance and stator inductance, respectively; E_α and E_β are the extend back EMF in the stationary coordinate system and satisfy:

$$\begin{bmatrix} E_\alpha \\ E_\beta \end{bmatrix} = \omega_e \lambda_f \begin{bmatrix} -\sin\theta_e \\ \cos\theta_e \end{bmatrix} \tag{2}$$

where λ_f is the permanent magnets flux linkage, and ω_e and θ_e are the electrical angular velocity and position angle, respectively.

According to Eq. (2), the extended EMF includes rotor position information, so the conventional SMO is constructed as follows:

$$\frac{d}{dt}\begin{bmatrix} \hat{i}_\alpha \\ \hat{i}_\beta \end{bmatrix} = \begin{bmatrix} -\frac{R}{L_s} & 0 \\ 0 & -\frac{R}{L_s} \end{bmatrix} \begin{bmatrix} \hat{i}_\alpha \\ \hat{i}_\beta \end{bmatrix} + \frac{1}{L_s}\begin{bmatrix} u_\alpha \\ u_\beta \end{bmatrix} - \frac{1}{L_s}\begin{bmatrix} k\cdot \mathrm{sign}(\tilde{i}_\alpha) \\ k\cdot \mathrm{sign}(\tilde{i}_\beta) \end{bmatrix} \tag{3}$$

Taking $\tilde{i}_\alpha = \hat{i}_\alpha - i_\alpha$ and $\tilde{i}_\beta = \hat{i}_\beta - i_\beta$ as sliding mode surfaces, the stator current error equation is obtained as follows:

$$\frac{d}{dt}\begin{bmatrix} \tilde{i}_\alpha \\ \tilde{i}_\beta \end{bmatrix} = \begin{bmatrix} -\frac{R}{L_s} & 0 \\ 0 & -\frac{R}{L_s} \end{bmatrix} \begin{bmatrix} \tilde{i}_\alpha \\ \tilde{i}_\beta \end{bmatrix} + \frac{1}{L_s}\begin{bmatrix} E_\alpha - k\cdot \mathrm{sign}(\tilde{i}_\alpha) \\ E_\beta - k\cdot \mathrm{sign}(\tilde{i}_\beta) \end{bmatrix} \tag{4}$$

where "$\hat{}$" denotes the estimated value, "$\sim$" the error, and k the gain of SMO. When the state variable reaches the sliding mode surface, the current error becomes zero, and the back EMF can be extracted using the sliding mode control law, as shown in Eq. (5):

$$\begin{bmatrix} E_\alpha \\ E_\beta \end{bmatrix} = \begin{bmatrix} k\cdot \mathrm{sign}(\tilde{i}_\alpha) \\ k\cdot \mathrm{sign}(\tilde{i}_\beta) \end{bmatrix} = \omega_e \lambda_f \begin{bmatrix} -\sin\theta_e \\ \cos\theta_e \end{bmatrix} \tag{5}$$

The sliding mode observer gain k satisfies: $k > \max\{-R|\tilde{i}_\alpha| + E_\alpha \mathrm{sgn}(\tilde{i}_\alpha), -R|\tilde{i}_\beta| + E_\beta \mathrm{sgn}(\tilde{i}_\beta)\}$. Since the discontinuous switching function is used to estimate the back EMF, an LPF is typically used to filter out the higher harmonics, and the arctangent function extracts the rotor position information.

$$\hat{\theta}_e = -\arctan(\hat{E}_\alpha / \hat{E}_\beta) \tag{6}$$

where $\hat{\theta}_e$ represents the estimated position angle, and $\hat{E}_\alpha$ and $\hat{E}_\beta$ are estimated values of back EMF along with α and β axes. The block diagram of conventional SMO is shown in Fig. 1.

3. PROPOSED FLUX SMO

3.1. Design of Flux SMO

The relationship between rotor flux linkages and rotor angle is:

$$\lambda = \begin{bmatrix} \lambda_\alpha \\ \lambda_\beta \end{bmatrix} = \lambda_f \begin{bmatrix} \cos\theta_e \\ \sin\theta_e \end{bmatrix} \tag{7}$$

where λ_α, λ_β are permanent magnet flux linkage along the α and β axes, respectively. Thus, the mathematical relationship between the back EMF and rotor flux linkages is further transformed as:

$$\begin{bmatrix} E_\alpha \\ E_\beta \end{bmatrix} = \omega_e \begin{bmatrix} -\lambda_\beta \\ \lambda_\alpha \end{bmatrix} \tag{8}$$

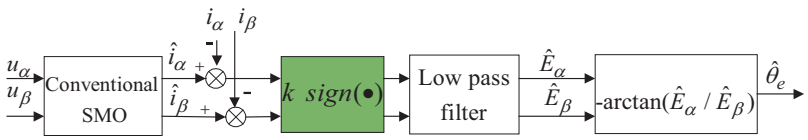

FIGURE 1. Block diagram of conventional SMO.

Therefore, Eq. (1) is further written as:

$$\begin{cases} \frac{di_\alpha}{dt} = -\frac{R}{L_s} i_\alpha + \frac{1}{L_s} u_\alpha + \frac{\omega_e}{L_s} \lambda_\beta \\ \frac{di_\beta}{dt} = -\frac{R}{L_s} i_\beta + \frac{1}{L_s} u_\beta - \frac{\omega_e}{L_s} \lambda_\alpha \end{cases} \tag{9}$$

In a current cycle, the mechanical time constant is greater than the electrical time constant, and the electrical angular velocity ω_e can be regarded as a constant, i.e., $\dot{\omega}_e = 0$. The rotor flux linkage equation is expressed as follows:

$$\frac{d}{dt} \begin{bmatrix} \lambda_\alpha \\ \lambda_\beta \end{bmatrix} = \begin{bmatrix} 0 & -\omega_e \\ \omega_e & 0 \end{bmatrix} \begin{bmatrix} \lambda_\alpha \\ \lambda_\beta \end{bmatrix} \tag{10}$$

Combining Eqs. (9) and (10), the extended state space equation taking stator current and rotor flux as variables can be written as

$$\frac{d}{dt} \begin{bmatrix} \mathbf{i} \\ \boldsymbol{\lambda} \end{bmatrix} = \begin{bmatrix} \mathbf{A}_{11} & \mathbf{A}_{12} \\ 0 & \mathbf{A}_{22} \end{bmatrix} \begin{bmatrix} \mathbf{i} \\ \boldsymbol{\lambda} \end{bmatrix} + \begin{bmatrix} \mathbf{B} \\ 0 \end{bmatrix} \begin{bmatrix} u_\alpha \\ u_\beta \end{bmatrix} \tag{11}$$

where $\mathbf{i} = [i_\alpha, i_\beta]^{\mathrm{T}}$ and $\boldsymbol{\lambda} = [\lambda_\alpha, \lambda_\beta]^{\mathrm{T}}$ are the stator current vector and rotor flux vector in the stationary coordinate system, respectively. The matrices are constructed as follows: $\mathbf{A}_{11} = \begin{bmatrix} -\frac{R}{L_s} & 0 \\ 0 & -\frac{R}{L_s} \end{bmatrix}$, $\mathbf{A}_{12} = \frac{1}{L_s} \begin{bmatrix} 0 & \omega_e \\ -\omega_e & 0 \end{bmatrix}$, $\mathbf{A}_{22} = \omega_e \mathbf{J}$, $\mathbf{J} = \begin{bmatrix} 0 & -1 \\ 1 & 0 \end{bmatrix}$, $\mathbf{B} = \frac{1}{L_s}\mathbf{I}$. Unlike the back EMF-based method, in this article, the rotor flux linkages are used as the observed object, so the FSMO is designed as:

$$\begin{aligned} \frac{d}{dt} \begin{bmatrix} \hat{\mathbf{i}} \\ \hat{\boldsymbol{\lambda}} \end{bmatrix} &= \begin{bmatrix} \mathbf{A}_{11} & \mathbf{A}_{12} \\ 0 & \mathbf{A}_{22} \end{bmatrix} \begin{bmatrix} \hat{\mathbf{i}} \\ \hat{\boldsymbol{\lambda}} \end{bmatrix} + \begin{bmatrix} \mathbf{B} \\ 0 \end{bmatrix} \begin{bmatrix} u_\alpha \\ u_\beta \end{bmatrix} \\ &+ \begin{bmatrix} \mathbf{I} \\ \mathbf{F} \end{bmatrix} \begin{bmatrix} -g \cdot \mathrm{sign}(\tilde{i}_\alpha) \\ -g \cdot \mathrm{sign}(\tilde{i}_\beta) \end{bmatrix} + \begin{bmatrix} \mathbf{H}_i \\ \mathbf{H}_\lambda \end{bmatrix} \end{aligned} \tag{12}$$

where $\mathbf{F} \in \mathbf{R}^{2\times 2}$ is the feedback matrix, and g represents the flux SMO gain. Subtracting Eq. (12) from Eq. (11), the observation error equation is as follows:

$$\begin{aligned} \frac{\mathrm{d}}{\mathrm{d}t} \begin{bmatrix} \tilde{\mathbf{i}} \\ \tilde{\boldsymbol{\lambda}} \end{bmatrix} &= \begin{bmatrix} \mathbf{A}_{11} & \mathbf{A}_{12} \\ 0 & \mathbf{A}_{22} \end{bmatrix} \begin{bmatrix} \tilde{\mathbf{i}} \\ \tilde{\boldsymbol{\lambda}} \end{bmatrix} \\ &+ \begin{bmatrix} \mathbf{I} \\ \mathbf{F} \end{bmatrix} \begin{bmatrix} -g \cdot \mathrm{sign}(\tilde{i}_\alpha) \\ -g \cdot \mathrm{sign}(\tilde{i}_\beta) \end{bmatrix} + \begin{bmatrix} \mathbf{H}_i \\ \mathbf{H}_\lambda \end{bmatrix} \end{aligned} \tag{13}$$

From Eq. (13), $\tilde{\mathbf{i}} = [\hat{i}_\alpha - i_\alpha, \hat{i}_\beta - i_\beta]^{\mathrm{T}}$ and $\tilde{\boldsymbol{\lambda}} = [\hat{\lambda}_\alpha - \lambda_\alpha, \hat{\lambda}_\beta - \lambda_\beta]^{\mathrm{T}}$ are the current and flux observation errors, respectively. If the system does not reach a steady state, i.e., the angular rate observing error is non-zero, the observing error matrix is calculated as follows: $\mathbf{H}_i = \Delta\mathbf{A}_{12} = (-1/L_s)\tilde{\omega}_e \mathbf{J}\hat{\boldsymbol{\lambda}}$, $\mathbf{H}_\lambda = \Delta A_{22} = \tilde{\omega}_e \mathbf{J}\hat{\boldsymbol{\lambda}}$.

3.2. Design of Feedback Matric

According to [21], a model reference adaptive system observer is used to estimate the rotor position angle. This method employs an error correction term as input to the observer, continuously minimizing the discrepancy between observed and actual currents. Following this consideration, the feedback matrix is required to form a closed loop of FSMO. This section presents the specific design steps. First, when the state variable is asymptotically stable on the sliding mode surface, the current observation errors should be zero. The equivalent control law is derived from the first variable of Eq. (13) as follows:

$$\mathbf{u}_{eq-i} = \begin{bmatrix} u_{eq-\alpha} \\ u_{eq-\beta} \end{bmatrix} = \begin{bmatrix} g \cdot \mathrm{sign}(\tilde{i}_\alpha) \\ g \cdot \mathrm{sign}(\tilde{i}_\beta) \end{bmatrix} = \mathbf{H}_i + \mathbf{A}_{12}\tilde{\boldsymbol{\lambda}} \tag{14}$$

Secondly, by substituting Eq. (14) into Eq. (13), the rotor flux differential equation can be further derived as:

$$\begin{aligned} \frac{d\tilde{\boldsymbol{\lambda}}}{dt} &= \mathbf{A}_{22}\tilde{\boldsymbol{\lambda}} + \mathbf{F}(-u_{eq-i}) + \mathbf{H}_\lambda \\ &= \mathbf{A}_{22}\tilde{\boldsymbol{\lambda}} + \mathbf{F}(-\mathbf{H}_i - \mathbf{A}_{12}\tilde{\boldsymbol{\lambda}}) + \mathbf{H}_\lambda \\ &= (\mathbf{A}_{22} - \mathbf{F}\mathbf{A}_{12})\tilde{\boldsymbol{\lambda}} + \mathbf{H}_\lambda - \mathbf{F}\mathbf{H}_i \end{aligned} \tag{15}$$

Substituting matrices $\mathbf{H}_i$ and $\mathbf{H}_\lambda$ into Eq. (15), Eq. (16) becomes:

$$\frac{\mathrm{d}\tilde{\boldsymbol{\lambda}}}{\mathrm{d}t} = \omega_e \mathbf{J}\mathbf{Q}\tilde{\boldsymbol{\lambda}} + \tilde{\omega}_e \mathbf{J}\mathbf{Q}\hat{\boldsymbol{\lambda}} \tag{16}$$

The expression of matrix $\mathbf{Q}$ is served as: $\mathbf{Q} = \mathbf{I} + \mathbf{F}\frac{1}{L_s}$, and $\mathbf{Q}$ is required to be equal to $l\mathbf{J}$. As a result, the feedback matrix can be written as:

$$\mathbf{F} = L_s(-\mathbf{I} + l\mathbf{J}) \tag{17}$$

where $l > 0$ is the feedback matrix gain. Substituting $\mathbf{Q} = l\mathbf{J}$ into Eq. (16), the equation of flux linkages errors can be obtained as follows:

$$\frac{d\lambda}{dt} + l\omega_e\tilde{\lambda} = -l\tilde{\omega}_e\hat{\lambda} \tag{18}$$

Eq. (18) can be written in the form of a transfer function as:

$$(s + l\omega_e)\tilde{\lambda} = -l\tilde{\omega}_e\hat{\lambda} \tag{19}$$

Eq. (19) shows that the pole of the flux SMO is $(-l\omega_e, 0)$ (where $l > 0$, the pole falls on the left half of the system, and the observer is asymptotically stable). The bandwidth of the observer is $l\omega_e$, and with the increase of l, the response speed increases, while the chatter phenomenon will be serious; with the decrease of l, the speed response decreases, with chatter reduction and robustness improvements.

If a suitable value of l is chosen, the estimated rotor angular velocity will gradually converge to the real value, while the observation error of the rotor flux linkages will be zero. As a result, the flux linkages along with α and β can be served as the objects to replace the back EMF, which realizes the decoupling of the flux linkages in the α and β axes. The overall diagram of the proposed flux SMO is shown as Fig. 2.

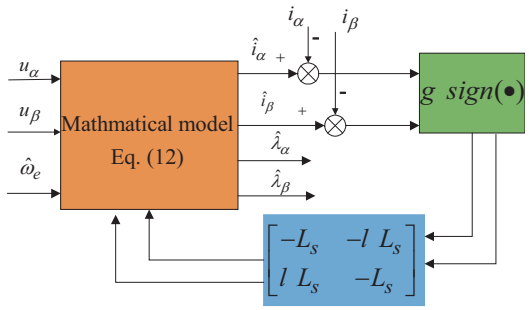

FIGURE 2. Block diagram of FSMO.

3.3. Stability Analysis of Flux SMO

The sliding mode gain g determines the convergence rate of the state variables, so designing the constant to ensure the stability of the proposed FSMO becomes critical. Typically, the Lyapunov function is used:

$$v = 0.5\tilde{\mathbf{i}}^{\mathrm{T}}\tilde{\mathbf{i}} = 0.5\left(\tilde{i}_\alpha^2 + \tilde{i}_\beta^2\right) \tag{20}$$

Differentiating Eq. (20) and bringing in the first-order equation of Eq. (13) yields

$$\dot{v} = \dot{\tilde{i}}_\alpha\tilde{i}_\alpha + \dot{\tilde{i}}_\beta\tilde{i}_\beta = -\frac{R}{L_s}(\tilde{i}_\alpha^2 + \tilde{i}_\beta^2) + \frac{\omega_e}{L_s}(\tilde{\lambda}_\beta\tilde{i}_\alpha - \tilde{\lambda}_\alpha\tilde{i}_\beta)$$

$$-g(\mathrm{sign}(\tilde{i}_\alpha)\tilde{i}_\alpha + \mathrm{sign}(\tilde{i}_\beta)\tilde{i}_\beta) \tag{21}$$

To meet the principle of asymptotic stability, there is a condition that the flux SMO gain g must satisfy:

$$g > \max\left\{\frac{\omega_e}{L_s}\tilde{\lambda}_\beta, \frac{\omega_e}{L_s}\tilde{\lambda}_\alpha\right\} \tag{22}$$

4. PROPOSED CPLL

4.1. Analysis of Conventional PLL Algorithm

Typically, extracted back EMFs from observers are fed into a PLL to estimate rotor position and speed, but high harmonics in the back EMF reduce estimation accuracy. Thus, [22] proposes a flux sliding mode observer combined with a conventional PLL (FSMO-PLL) for improved sensorless control. The following section provides a detailed explanation of the conventional PLL algorithm, and the block diagram of the conventional PLL is illustrated in Fig. 3.

The rotor flux linkages inherently contain information about the rotor position. To establish the relationship between the rotor flux linkages and rotor position, the expression for the rotor

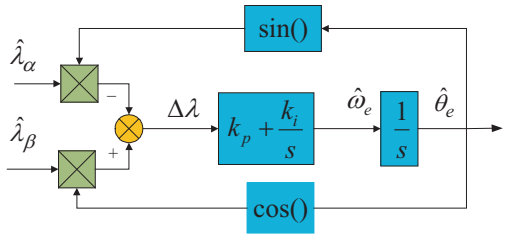

FIGURE 3. Block diagram of conventional PLL.

flux linkages is written as:

$$\hat{\boldsymbol{\lambda}} = \begin{bmatrix} \hat{\lambda}_\alpha \\ \hat{\lambda}_\beta \end{bmatrix} = \hat{\lambda}_f \begin{bmatrix} \cos\theta_e \\ \sin\theta_e \end{bmatrix} \tag{23}$$

where $\hat{\lambda}_f$ represents the estimated value of permanent magnets flux linkage. As shown in Fig. 3, $\hat{\omega}_e$ and $\hat{\theta}_e$ are estimates of the electrical angular velocity and rotor angle, respectively, and the position error signal $\Delta\lambda$ can be derived as:

$$\Delta\lambda = \hat{\lambda}_f \sin(\theta_e - \hat{\theta}_e) \tag{24}$$

To improve rotor movement velocity, assume that:

$$\Delta\theta = \sin(\theta_e - \hat{\theta}_e) = \theta_e - \hat{\theta}_e \tag{25}$$

Therefore, Eq. (24) can be transformed into Eq. (26):

$$\Delta\lambda = \hat{\lambda}_f\Delta\theta \tag{26}$$

By analyzing the structure of the conventional PLL, the transfer function between the estimated position and real position is obtained:

$$G(s) = \frac{\hat{\theta}_e}{\theta_e} = \frac{\hat{\lambda}_f(k_p s + k_i)}{s^2 + \hat{\lambda}_f k_p s + \hat{\lambda}_f k_i} \tag{27}$$

where k_p and k_i are proportionality and integration coefficients, respectively.

4.2. Analysis of CPLL Algorithm

The principle of proposed CPLL: To enhance the performance of the sensorless control system for PMSMs, this section outlines the specific steps of the proposed CPLL. Firstly, a pre-filter is applied to filter out the harmonics present in the rotor flux linkages, and the filtered flux linkages are then fed into the CPLL. A reference speed is added to the integral controller to improve the dynamic performance of the CPLL. Immediately, the estimated electrical angular velocity is fed into the pre-filter stage with the objective of reducing the rotor flux's high harmonics. The whole position estimation process is shown in Fig. 4.

As shown in Fig. 4, the extracted fundamental rotor flux linkages equation is expressed as:

$$\begin{cases} \hat{\lambda}_{b\alpha} = \hat{\lambda}_{f1}\cos(\theta_m) \\ \hat{\lambda}_{b\beta} = \hat{\lambda}_{f1}\sin(\theta_m) \end{cases} \tag{28}$$

where $\hat{\lambda}_{b\alpha}$ and $\hat{\lambda}_{b\beta}$ are the filtered flux linkages along the α and β axes; $\hat{\lambda}_{f1}$ is the fundamental amplitude of the filtered rotor

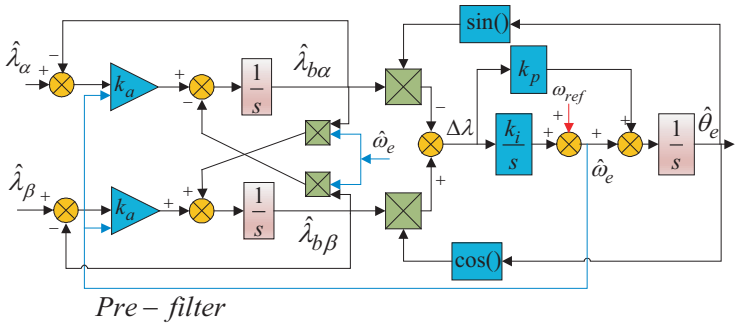

FIGURE 4. Block diagram of CPLL.

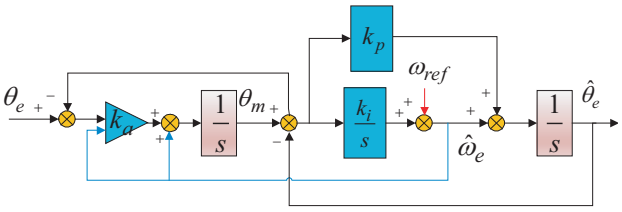

FIGURE 5. The linearized model of CPLL.

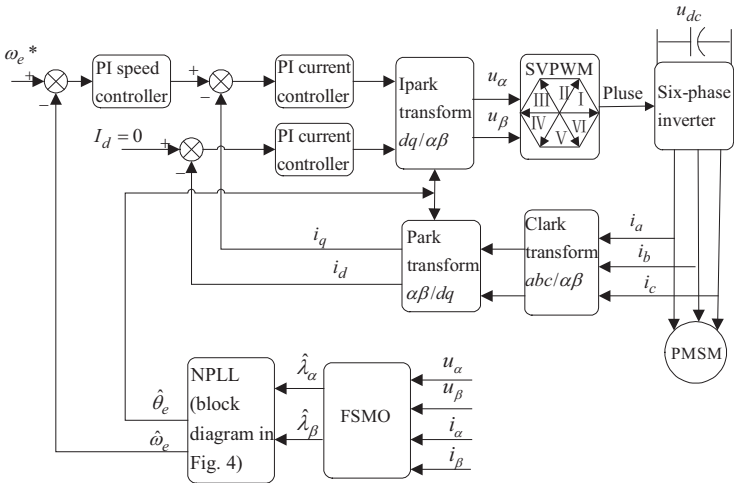

FIGURE 6. Block diagram of the sensorless FOC based on the proposed method.

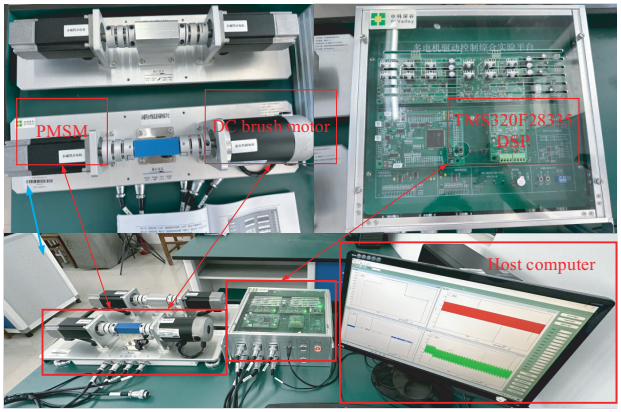

FIGURE 7. Experimental platform.

flux linkages; θ_m is the phase tracking angle. Differentiating Eq. (28), the expression containing the position information is obtained as follows:

$$\begin{cases} \theta_m = \tan^{-1}(\hat{\lambda}_{b\beta}/\hat{\lambda}_{b\alpha}) \\ p\theta_m = (-(p\hat{\lambda}_{b\alpha})\hat{\lambda}_{b\beta} + (p\hat{\lambda}_{b\beta})\hat{\lambda}_{b\alpha})/\hat{\lambda}_{f1}^2 \end{cases} \tag{29}$$

where p represents the differential operator. Furthermore, the differential equation for the prefilter link can be written as:

$$\begin{cases} p\hat{\lambda}_{b\alpha} = k_a\hat{\omega}_e(\hat{\lambda}_\alpha - \hat{\lambda}_{b\alpha}) - \hat{\omega}_e\hat{\lambda}_{b\beta} \\ p\hat{\lambda}_{b\beta} = k_a\hat{\omega}_e(\hat{\lambda}_\beta - \hat{\lambda}_{b\beta}) + \hat{\omega}_e\hat{\lambda}_{b\alpha} \end{cases} \tag{30}$$

Eq. (23) is used as the input of CPLL, and assuming that $\theta_e = \theta_m$, $\hat{\lambda}_f = \hat{\lambda}_{f1}$, combining Eqs. (28)–(30), Eq. (29) can be transformed to Eq. (31):

$$\begin{aligned} p\theta_m &= \hat{\omega}_e + k_a\hat{\omega}_e\sin(\theta_e - \theta_m) \\ &\approx \hat{\omega}_e + k_a\hat{\omega}_e(\theta_e - \theta_m) \end{aligned} \tag{31}$$

The linearized model of the CPLL is shown in Fig. 5, and the control system's closed-loop transfer function is

$$\frac{\hat{\theta}_e}{\theta_e} = \frac{k_a k_p\hat{\omega}_e s + k_a k_i\hat{\omega}_e}{s^3 + (k_a\hat{\omega}_e + k_p)s^2 + k_a k_p\hat{\omega}_e s + k_a k_i\hat{\omega}_e} \tag{32}$$

As the transfer function of the third-order dynamic system, if the system is kept stable, the appropriate function should be chosen so that the pole falls in the left half plane. According to the stability principle, the appropriate polynomial is chosen as follows:

$$M(s) = (s+n)(s^2 + 2\xi\omega_n s + \omega_n^2) \tag{33}$$

where n is the root of this function, which should satisfy $n > 0$; ζ is damping coefficient of 0.707; ω_n represents center angular frequency and is set to $0.3\omega_e$. If the appropriate parameters of k_p and k_i are selected, the observed position angle will synchronize with the actual value.

5. PMSM SENSORLESS FOC STRUCTURE AND HARDWARE CONFIGURATION

In this paper, the FOC method with $i_d = 0$ is used to simplify the stator current, and proportional-integral (PI) controllers are used uniformly in the speed and current loops. Space vector pulse width modulation is used to generate pulses, which are then converted into three-phase sinusoidal waveforms by the inverter. More importantly, the conventional SMO-PLL method and the method of FSMO-PLL are used to demonstrate the superiority of the proposed method. The overall diagram of the proposed FSMO-CPLL for PMSM sensorless control is shown in Fig. 6. Simulation models are built using MATLAB/Simulink, with specific parameters listed in Table 1.

Figure 7 depicts an experimental platform using the TMS320F28335 DSP. It consists of four main parts: the

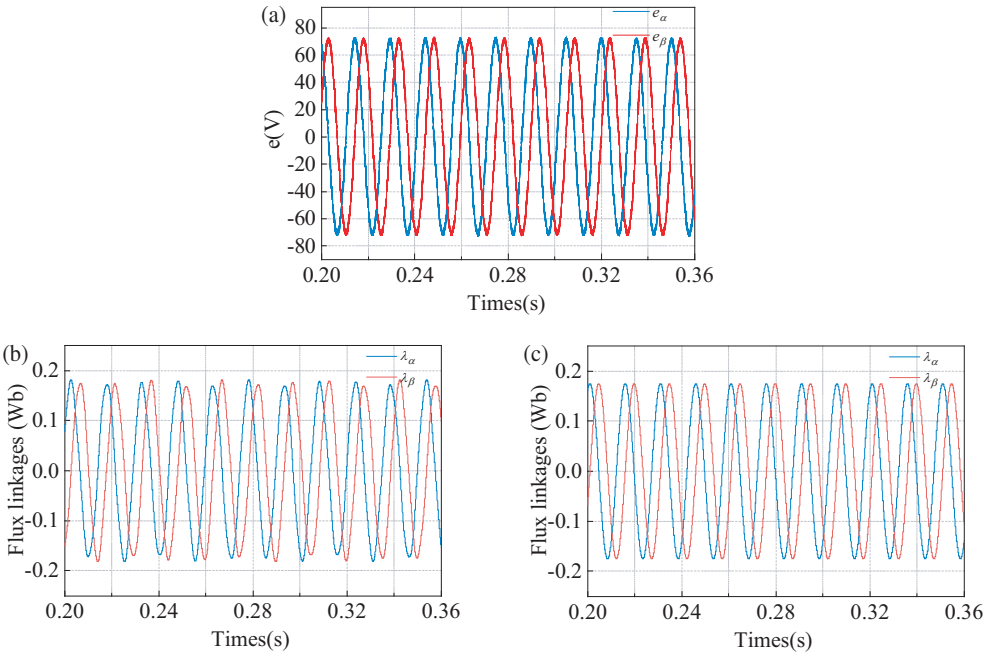

FIGURE 8. Estimation results of the back EMF and flux linkages using (a) SMO-PLL, (b) FSMO-PLL, (c) FSMO-CPLL.

PMSM and DC brushless motor pair of bracket platforms, drive control test box, torque sensor, and cSPACE host computer. In addition, a 2500-line incremental encoder is integrated to detect position and speed, as well as provide velocity compensation for the CPLL. Table 2 shows the experimental parameters of the PMSM.

TABLE 1. FSMO and CPLL parameters.

Parameters	Values	Notes
g	1000	Sliding mode surface gain
l	3	Feedback matrix coefficient
k_a	0.707	Prefilter gain
k_p	-15	Proportion coefficient of CPLL
k_i	-30	Integral coefficient of CPLL

TABLE 2. Experimental parameters of PMSM.

Parameters	Values	Notes
U_{dc}	4.8 V	Rated voltage
T_e	1.27 N · m	Rated torque
n	4500 rpm	Maximum speed
I	12.5 A	Rated current
J	0.00003 kg · m^2	Rotational inertia
R_s	0.25 Ω	Stator resistance
L_d	0.5 mH	d axis inductance
L_q	0.5 mH	q axis inductance

6. SIMULATION RESULTS AND EXPERIMENT VERIFICATION

6.1. Simulation Results

1) Comparative results for medium and high PMSM speeds: In this section, the effectiveness of the proposed control strategy is evaluated under the condition that the motor runs at 1000 rpm.

Figures 8(a), 8(b), and 8(c) show the estimated back EMF of the SMO PLL, as well as the rotor flux of the FSMO-PLL and FSMO-CPLL. Figs. 9(a), 9(b), and 9(c) show the Fast Fourier Transform (FFT) in the three methods. The results show that at the fundamental frequency of 60 Hz, the total harmonic distortions in the SMO-PLL and FSMO-PLL are 66.66% and 35.92%, respectively, while in the FSMO-CPLL, the total harmonic distortion is 33.29%, which is reduced by 50.1% and 7.3%. It can be explained that the high harmonics in the rotor flux linkages are effectively suppressed due to the intrinsic filtering properties of the FSMO, whereas the LPF in conventional SMO is not well adapted to different systems by setting a low-pass cutoff frequency.

Figures 10(a)–(c) are the rotor position and estimation error profiles for SMO-PLL, FSMO-PLL, and FSMO-CPLL, respectively. Fig. 10(a) demonstrates that the observed rotor position angle has a significant phase lag, with an observation error of approximately 0.5 rad. In Figs. 10(b) and 10(c), there is a significant overlap between the estimated and real values, and the estimation error for both is close to 0 rad. Additionally, the estimation error with the FSMO-CPLL is smoother, indicating that the rotor position is more stable. In conclusion, the proposed CPLL with angular compensation significantly improves the accuracy of the extracted position, aligning with the theoretical analysis presented in Section 3.

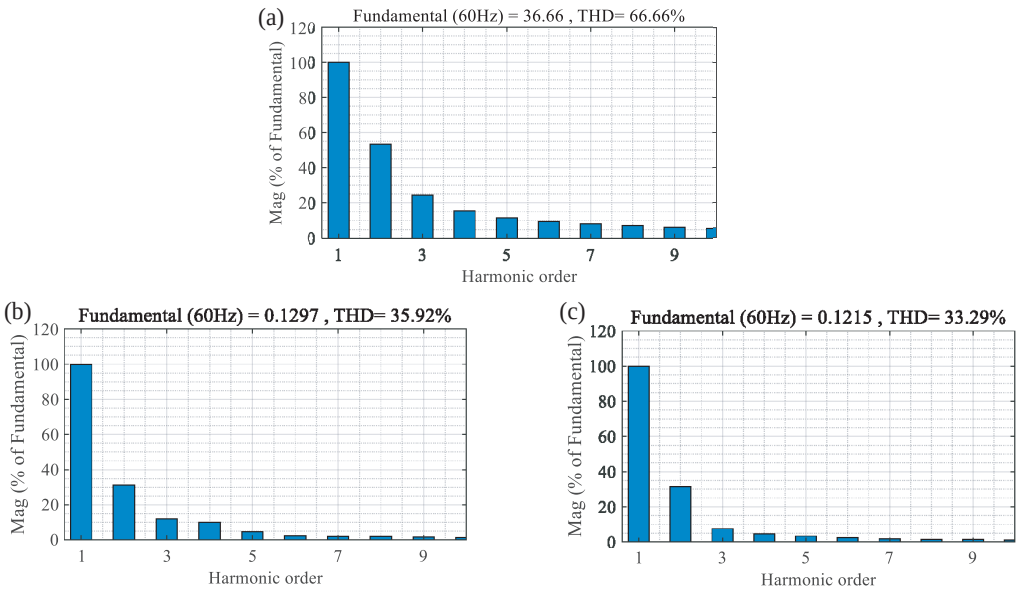

FIGURE 9. Harmonic analyses of back EMF and flux linkages using (a) SMO-PLL, (b) FSMO-PLL, (c) FSMO-CPLL.

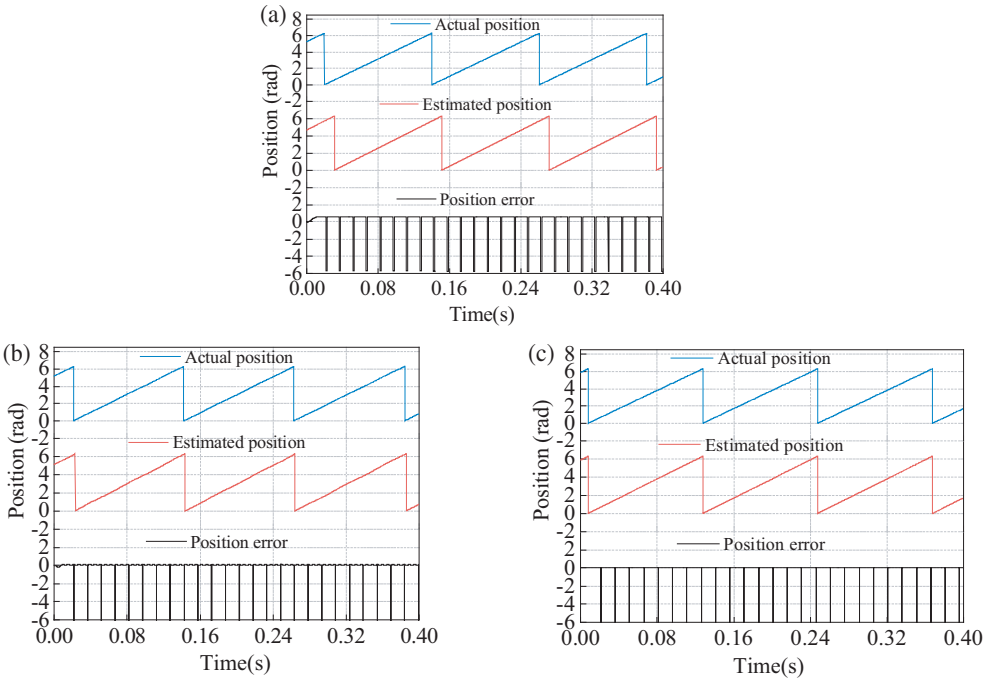

FIGURE 10. Position and estimation errors at a speed of 1000 rpm using (a) SMO-PLL, (b) FSMO-PLL, (c) FSMO-CPLL.

2) Comparative results at relatively low PMSM speeds: To further validate the effectiveness of the proposed control strategy, the estimation results with the motor running at a lower speed of 500 are shown in Figs. 11(a)–(c).

The start-up process is first analyzed using the same PI controller. According to Figs. 11(a) and 11(b), the speed curves overshoot to some extent when using the SMO-PLL and FSMO-PLL; the overshoot amount for both methods is nearly 200 rpm, and the maximum estimation errors for them are 290 rpm and 250 rpm, respectively. In Fig. 11(c), the overshoot amount is reduced to 50 rpm, and the speed estimation error is almost 0 rpm.

Furthermore, when the motor has reached a steady state, there is a little chatter in the SMO-PLL and FSMO-PLL. When using the FSMO-CPLL, the high harmonics of the rotor flux linkages are filtered out before speed estimation, resulting in an estimated speed that is nearly identical to the real one. When a load of 10 Nm is applied in 0.2 s, the absolute values of the estimation errors in the SMO-PLL and the FSMO-PLL are around 72 rpm and 20 rpm, respectively, while the maximum error remains stable at 0 rpm in the FSMO-CPLL.

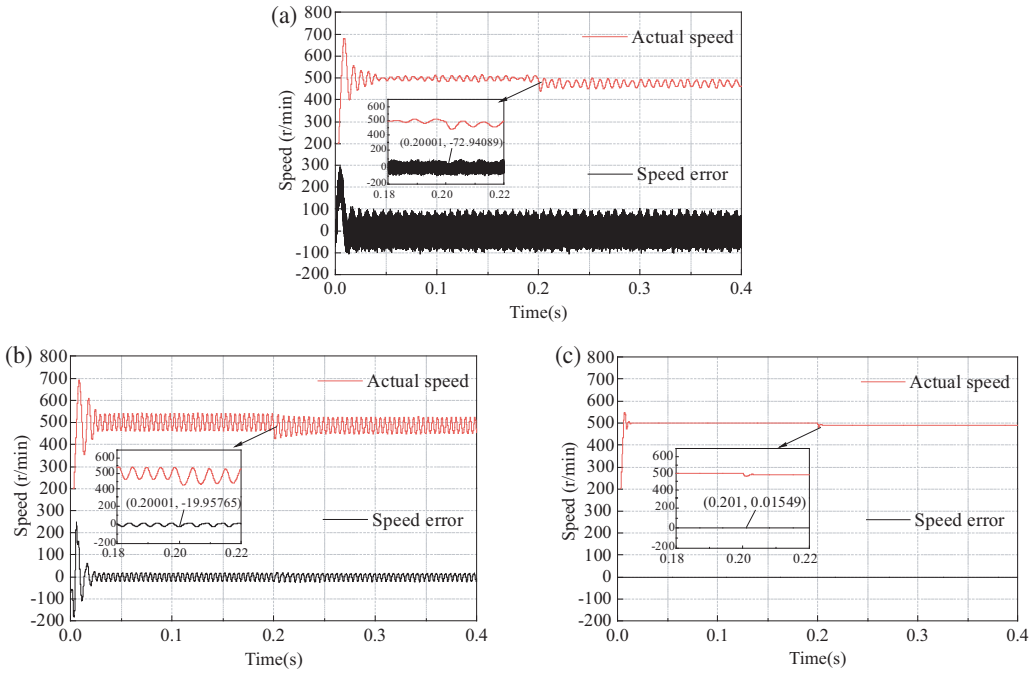

FIGURE 11. Speed and estimation errors at a speed of 500 rpm with a sudden load of 10 N · m at 0.2 s using (a) SMO-PLL, (b) FSMO-PLL, (c) FSMO-CPLL.

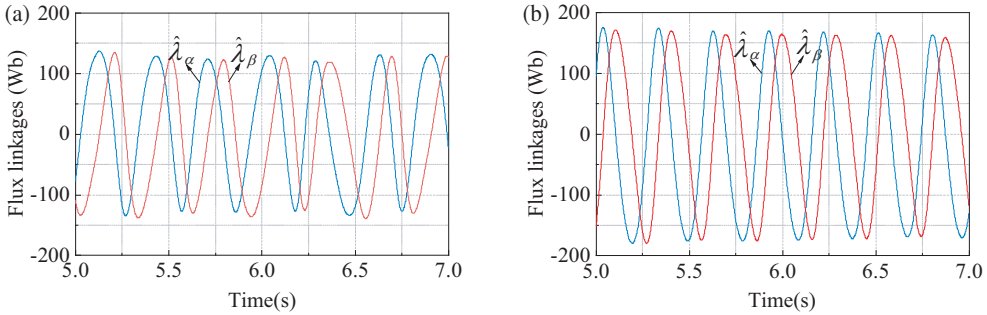

FIGURE 12. Estimation results of flux linkages using (a) FSMO-PLL, (b) FSMO-CPLL at a low-speed operation of 50 rpm.

In conclusion, the high harmonic distortion in FSMO-CPLL is reduced by 50.1% and 7.3%, respectively, while the position estimation accuracy has been greatly improved due to a lower phase lag. Moreover, the starting performance and load-carrying ability have been significantly improved compared to the SMO-PLL and FSMO-PLL. Therefore, the proposed FSMO-CPLL for PMSM sensorless control is extremely important, whether at medium and high or low speeds.

6.2. Experiment Results

1) Steady state performance validation: This section presents the experiment results for FSMO-PLL and FSMO-CPLL, with the motor running at 50 rpm and starting with no load. Figs. 12(a) and 12(b) show the estimation results for flux linkages in the FSMO-PLL and FSMO-CPLL. The results demonstrate that when the two strategies are applied to an actual motor operation, the obtained flux linkages take the form of sinusoidal stable changes, which is consistent with simulation results. The difference is that the larger the flux amplitude is in FSNO-CPLL, the more stable the system is, as evidenced by the smaller jumps in the rotor flux linkages in Fig. 12(b).

Figures 13(a) and 13(b) depict the results of speed and estimation errors in the FSMO-PLL and FSMO-CPLL. Obviously, the absolute value of estimation errors in Fig. 13(a) reach approximately 25 rpm, whereas in Fig. 13(b), the speed profile is basically consistent with the real one, with the maximum estimation errors of no more than 4 rpm. The larger the speed fluctuation is, the more the system chatters are, indicating that the FSMO-CPLL outperforms the FSMO-PLL in maintaining position stability.

Figures 14(a) and 14(b) depict position and estimation errors in FSMO-PLL and FSMO-CPLL. The experimental results within 3–6 s show that the estimated rotor position in Fig. 14(a) has a significant hysteresis, and the delay of this method is about one cycle, whereas in Fig. 14(b), the phase delay is reduced by half. Furthermore, the estimation errors in Fig. 14(b) follow a regular pattern, ranging from -4 to 3 rad. Conversely,

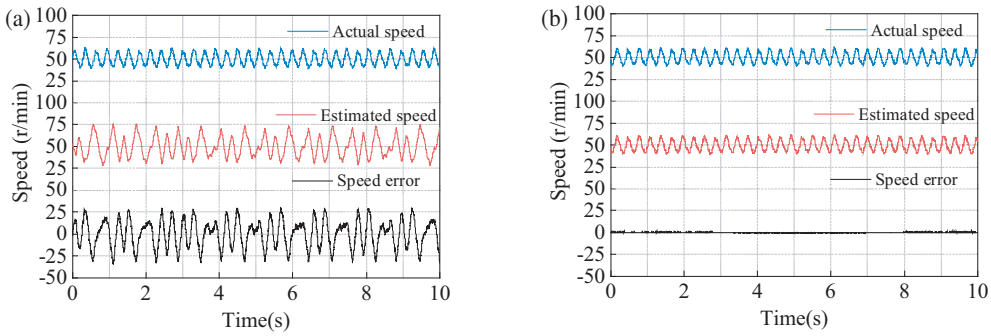

FIGURE 13. Speed and estimation errors at a speed of 50 rpm using (a) FSMO-PLL, (b) FSMO-CPLL.

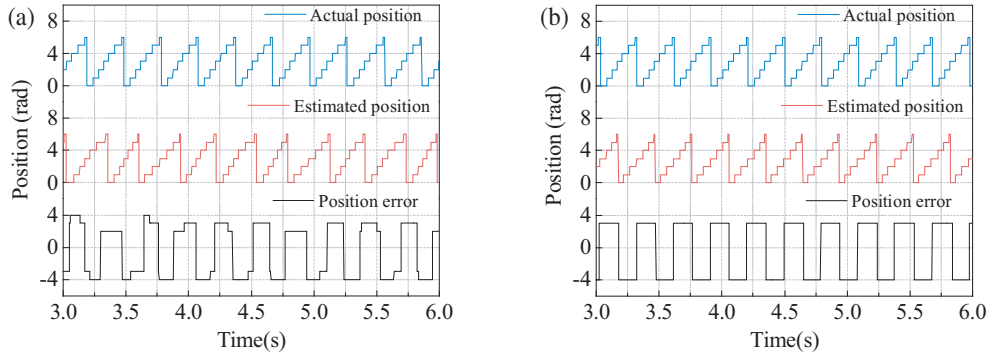

FIGURE 14. Position and estimation errors using (a) FSMO-PLL, (b) FSMO-CPLL.

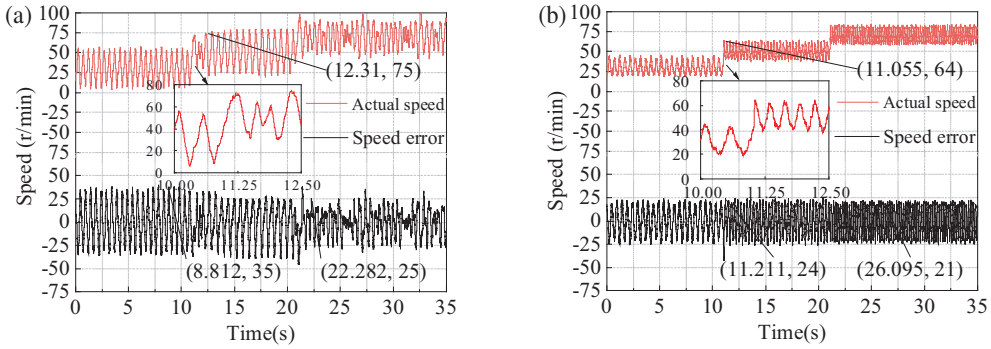

FIGURE 15. Estimation results of speed using (a) FSMO-PLL, (b) FSMO-CPLL at an increase in speed from 30 rpm to 50 rpm, then to 70 rpm.

the estimation errors are almost exceeding 3 rad with an irregular shape, as shown in Fig. 14(a). The irregular variation of estimation errors in the FSMO-PLL reflects the vicious chattering of rotor position, which is reduced by the FSMO-CPLL.

To summarize the experimental results, Table 3 compares the proposed FSMO-CPLL method with FSMO-PLL method. The results show that using the FSMO-CPLL method for sensorless control of PMSM significantly reduces phase delay, achieves the lowest maximum speed error, and provides the most stable rotor position.

2) Dynamic performance verification: Due to the motor's uncertainty in various conditions, the effectiveness of the proposed method in a dynamic environment has yet to be verified. Fig. 15 shows the speed estimation results obtained using FSMO-PLL and FSMO-CPLL as the motor speed increased from 30 rpm to 50 rpm and then to 70 rpm. According to Fig. 15(b), as the motor speed increases, the estimation errors become more compact and show a decreasing trend; the fluctuation range is between 24 and 21 rpm, with a maximum estimation error of no more than 25 rpm. According to Fig. 15(a), although the estimation errors decrease as the motor speed increases, the instability of the rotor position occurs, shown as the fluctuation range of 34–25 rpm, and the maximum estimation errors occur at around 35 rpm.

The comparison of Figs. 15(a) and 15(b) indicates that the higher the speed is, the better the dynamic performance of the motor is in both methods. The difference is that in FSMO-CPLL, the rotor behaves more consistently, resulting in greater PMSM control accuracy. In addition, as the speed increases from 30 to 50 rpm, the FSMO-PLL's response time is approxi-

TABLE 3. Comparison of experimental results of two method.

Control Methods	Phase Delay (cycle)	Position Error Range (rad)	Maximum Speed Error (rpm)
FSMO-PLL	1	−4 to 4	25
FSMO-CPLL	0.5	−4 to 3	4

mately 2.31 s, while the response time for FSMO-CPLL is only 1.06 s, resulting in a 54.1% improvement in system response. The same happens when the speed increases from 50 to 70 rpm. Therefore, the proposed FSMO-CPLL achieves faster dynamic performance with less speed fluctuation, making it an effective strategy for PMSM drives.

7. CONCLUSION

This paper proposes a compensated PLL controller in conjunction with an FSMO for PMSM sensorless drives. By considering harmonics in FSMO, a feedback matrix is constructed to enhance the accuracy of flux linkages observation, thereby replacing the conventional LPF. To reduce phase lag, the angular rate compensation strategy is applied to the conventional PLL to improve position accuracy. Both simulated and experimental results demonstrate that the proposed method significantly reduces rotor fluctuations and effectively filters out high harmonics. Notably, even at low operating conditions of the PMSM, the proposed method achieves a 50% reduction in phase delay and a 16% suppression of speed fluctuations compared to FSMO-PLL method.

Due to the sensitivity of flux linkages, only experimental validation of the proposed sensorless method for low-speed motor operation is performed. Therefore, our future research should focus on two aspects: 1) Improving the performance of the observer so that it can be applied to medium- and high-speed domains. 2) Combining this sensorless control method with the speed loop to improve the speed adaptive rate of the FSMO.

ACKNOWLEDGEMENT

This work was supported in part by the Anhui Provincial Natural Science Foundation under Grant No. 2108085MF200, in part by the National Natural Science Foundation of China under Grant No. 62071004, and in part by the Natural Science Research Project of Anhui Educational Committee under Grant No. 2022AH051583.

REFERENCES

[1] Li, K., L. Wang, and Y. Zhu, "An active flux model-based sensorless flux weakening control algorithm for permanent magnet synchronous motors," *Progress In Electromagnetics Research Letters*, Vol. 116, 39–45, 2024.

[2] Wu, L., Z. Lyu, Z. Chen, J. Liu, and Y. Lu, "An enhanced sensorless control scheme for PMSM drives considering self-inductance asymmetry," *CES Transactions on Electrical Machines and Systems*, Vol. 6, No. 4, 384–392, 2022.

[3] Bi, G., G. Zhang, Q. Wang, D. Ding, B. Li, G. Wang, and D. Xu, "High-frequency injection angle self-adjustment based online position error suppression method for sensorless PMSM drives," *IEEE Transactions on Power Electronics*, Vol. 38, No. 2, 1412–1417, 2023.

[4] Sun, X., Y. Zhang, X. Tian, J. Cao, and J. Zhu, "Speed sensorless control for IPMSMs using a modified MRAS with gray wolf optimization algorithm," *IEEE Transactions on Transportation Electrification*, Vol. 8, No. 1, 1326–1337, 2022.

[5] Bian, Y., Z. Yang, X. Sun, and X. Wang, "Speed sensorless control of a bearingless induction motor based on modified robust kalman filter," *Journal of Electrical Engineering & Technology*, Vol. 19, No. 3, 1179–1190, 2024.

[6] Bai, H. and B. Yu, "Position estimation of fault-tolerant permanent magnet motor in electric power propulsion ship system," *IEEJ Transactions on Electric and Electronic Engineering*, Vol. 17, No. 6, 890–898, 2022.

[7] Sun, Q., X. Zhu, and F. Niu, "Sensorless control of permanent magnet synchronous motor based on new sliding mode observer with single resistor current reconstruction," *CES Transactions on Electrical Machines and Systems*, Vol. 6, No. 4, 378–383, 2022.

[8] Ding, L., Y. W. Li, and N. R. Zargari, "Discrete-time SMO sensorless control of current source converter-fed PMSM drives with low switching frequency," *IEEE Transactions on Industrial Electronics*, Vol. 68, No. 3, 2120–2129, 2021.

[9] Xu, Y., C. Wang, W. Yuan, Z. Li, and Z. Yin, "Anti-disturbance position sensorless control of PMSM based on improved sliding mode observer with suppressed chattering and no phase delay," *Journal of Electrical Engineering & Technology*, Vol. 18, No. 4, 2895–2907, 2023.

[10] Yin, Z., Y. Zhang, X. Cao, D. Yuan, and J. Liu, "Estimated position error suppression using novel PLL for IPMSM sensorless drives based on full-order SMO," *IEEE Transactions on Power Electronics*, Vol. 37, No. 4, 4463–4474, 2022.

[11] Xu, W., Y. Jiang, C. Mu, and F. Blaabjerg, "Improved nonlinear flux observer-based second-order SOIFO for PMSM sensorless control," *IEEE Transactions on Power Electronics*, Vol. 34, No. 1, 565–579, 2019.

[12] Ye, S., "Design and performance analysis of an iterative flux sliding-mode observer for the sensorless control of PMSM drives," *ISA Transactions*, Vol. 94, 255–264, 2019.

[13] Ye, S. and X. Yao, "A modified flux sliding-mode observer for the sensorless control of PMSMs with online stator resistance and inductance estimation," *IEEE Transactions on Power Electronics*, Vol. 35, No. 8, 8652–8662, 2020.

[14] Wang, G. and H. Zhang, "A new speed adaptive estimation method based on an improved flux sliding-mode observer for the sensorless control of PMSM drives," *ISA Transactions*, Vol. 128, 675–685, 2022.

[15] Ge, Y., W. Song, Y. Yang, and P. Wheeler, "A polar-coordinate-multisignal-flux-observer-based PMSM non-PLL sensorless control," *IEEE Transactions on Power Electronics*, Vol. 38, No. 9, 10 579–10 583, 2023.

[16] Yan, H., W. Wang, Y. Xu, and J. Zou, "Position sensorless control for PMSM drives with single current sensor," *IEEE Transactions on Industrial Electronics*, Vol. 70, No. 1, 178–188, 2023.

[17] Song, X., J. Fang, B. Han, and S. Zheng, "Adaptive compensation method for high-speed surface PMSM sensorless drives of EMF-based position estimation error," *IEEE Transactions on Power Electronics*, Vol. 31, No. 2, 1438–1449, 2016.

[18] Zhao, W., S. Song, and S. Zhou, "Current source inverter driven PMSM position sensorless control with improved sliding mode observer," *Journal of Electrical Technology*, Vol. 39, No. 4, 987–995, 2024.

[19] Novak, Z. and M. Novak, "Adaptive PLL-based sensorless control for improved dynamics of high-speed PMSM," *IEEE Transactions on Power Electronics*, Vol. 37, No. 9, 10 154–10 165, 2022.

[20] Liu, G., H. Zhang, and X. Song, "Position-estimation deviation-suppression technology of PMSM combining phase self-compensation SMO and feed-forward PLL," *IEEE Journal of Emerging and Selected Topics in Power Electronics*, Vol. 9, No. 1, 335–344, 2021.

[21] Liu, Z.-H., J. Nie, H.-L. Wei, L. Chen, F.-M. Wu, and M.-Y. Lv, "Second-order ESO-based current sensor fault-tolerant strategy for sensorless control of PMSM with B-phase current," *IEEE/ASME Transactions on Mechatronics*, Vol. 27, No. 6, 5427–5438, 2022.

[22] Ye, S., "A novel fuzzy flux sliding-mode observer for the sensorless speed and position tracking of PMSMs," *Optik*, Vol. 171, 319–325, 2018.